

NOISE GENERATION AROUND NACA0012 WINGTIP USING LARGE-EDDY-SIMULATION

Taro IMAMURA*, Shuji ENOMOTO*, and Kazuomi YAMAMOTO*

*Japan Aerospace Exploration Agency

Keywords: Aerodynamics, Aeroacoustics, Computational Fluid Dynamics, High Lift Devices

Abstract

A flow around NACA0012 wingtip is solved using a zonal LES/RANS hybrid method in order to understand the noise generation mechanism around the flap-edge. It is known from the previous studies that the flow around the blunt wingtip is similar to that of the flap-edge. Grid dependency studies are performed for both time-averaged and unsteady components and the results are assessed by comparing with the experimental data. It became apparent that zonal LES/RANS hybrid results are more sensitive to the chordwise grid resolution, compared with that of RANS. Using the validated data, the noise generation mechanism around the wingtip is discussed. The near-field flow structures relevant to noise generation are obtained successfully.

1 Introduction

Over the past few decades, aircraft noise has become one of the major problems due to the increase in air travel. FAA regulation on noise around airport is becoming more stringent than ever, and it is clear that noise reduction technology is critical to the future commercial aircraft development. Since engine noise has been declining during the last few decades, the airframe noise can no longer be ignored for the purpose of further noise reduction. This is especially true for the case of flow around high lift devices (HLD) during the landing phase, which generates noise at the level comparative to that produced by engines, because at this condition the engines are driven at low power

[1]. From the previous studies, it is well known that the sound generated from the flap-edge is one of the causes for the airframe noise [2]. However, it seems to be difficult to simulate the aerodynamic fluctuations which lead to the noise generation around the flap. Most of the computations done in the past were based on Reynolds Averaged Navier-Stokes (RANS) equations [2-7], which basically assumed a steady-state flow. Recently, Cummings *et al.* [8] calculated a flow around three dimensional three-element HLD configuration using detached eddy simulation (DES), and qualitative comparison were made for the power spectrum density of wing lift. However, it seems to be difficult to reproduce the aerodynamic fluctuations which lead to the noise generation around the flap.

Thus, the objective of this study is to get further information related with the noise sources around the flap of HLD by performing accurate unsteady flow simulations, and estimated the noise sources around the flap-edge. However, unsteady computations around the flap of HLD are not feasible yet. Therefore, careful consideration should be made before approaching this objective. McInerny *et al.* [9] performed wind tunnel experiments of a blunt-tipped rectangular wing with NACA0012 airfoil section, and showed that the flow structure can be correlated closely with that of the flap-edge. Also, in our previous study [10], similarity of the steady-state flow field around NACA0012 wingtip and that of the flap-edge was assessed using Reynolds-averaged Navier-Stokes (RANS) methods. Based on these studies, this simple configuration is expected to have a

similar noise generating mechanism as that of the flap-edge.

Based on the previous discussions, a zonal LES/RANS hybrid method is applied to solve the unsteady vortical flow structures around the wingtip. Unsteady computations are performed varying the grid resolutions. The results are compared with the wind tunnel experiment performed at Japan Aerospace Exploration Agency (JAXA). Using the validated numerical data, detail observation of the flow structure around the wingtip is performed. Finally, far field Sound Pressure Level (SPL) estimation based on Curle's equation is presented using the unsteady surface data as an input.

This paper is organized as follows. Section 2 briefly describes the computational model, numerical methods and setup of the simulations. Section 3 presents the computational results. The computed steady and unsteady components are presented. Especially, the unsteady components are compared with the experiment varying the grid resolution. Based on the validated data, the flow field around the wingtip region is observed in detail. Finally, section 4 concludes this paper.

2 Numerical Setup

2.1 Computational Model and Flow Conditions

The computational model is based on the experiment performed at Low-speed Wind Tunnel in JAXA (JAXA-LTW2) [11-12], which is a closed-circuit wind tunnel with a $2m \times 2m$ cross section. The model is a rectangular wing having NACA0012 profile as shown in Fig. 1. The shape of the wingtip is blunt, which has sharp edges. The size of the model is 0.4m in chord and 1.0m in span. The test was carried out to provide the experimental data for CFD validation and to know flow physics around the near field of the wingtip.

The flow conditions for the computations were selected as follows. The mean flow velocity is 60m/s, which corresponds to Mach number of 0.175. This flow velocity is similar to that of the landing speed of the aircraft. In order

to mimic the flow field of the flap-edge, high angle-of-attack is desirable. In the experiment, however, flow separation was observed near the trailing edge over angle-of-attack of 12 degrees. In order to focus only on the noise generation at the wingtip, angle-of-attack of 12 degrees is chosen. The Reynolds number, based on the chord length (c) and mean flow velocity (U_∞) is 1.8×10^6 .



Fig. 1. NACA0012 Wingtip Mounted inside the Wind Tunnel

2.2 Computational Grids

Block-structured one-to-one point-matched grid was generated with the commercial software Gridgen and the grid topology is shown in Fig. 2. As shown in Fig. 2, x -, y -, and z -directions correspond to the chordwise, spanwise, and vertical directions, respectively.

Two grids are used in this study and the details are summarized in Table 1. The first grid consists of nearly 6 million grid points and will be called 6M grid hereafter. In the previous studies, it is known that vortices of x (chordwise) component around the wingtip region play important roles. Thus, fine and uniform grid on the chordwise cross section is generated as shown in the left side of Fig 3 (a). The fine and uniform grid distribution is achieved inside the region where the distance from the wall is smaller than $0.1c$. On the other hand, the grid distribution along the chordwise direction is coarser than that of the cross sectional plane as shown in Fig 3 (b). The

second grid consists of approximately 20 million grid points and will be called 20M grid hereafter. This grid was designed to overcome the defect of the 6M grid. The grid resolution on the chordwise cross sectional plane is almost the same as 6M grid (See Fig. 4 (a)). The fine grid region is extended to $0.15c$ for 20M grid in spanwise direction and also in the vertical direction at the trailing edge. The grid size in chordwise direction is nearly 4 times smaller than 6M grid around the mid-chord location. Consequently, the grid sizes in all directions around the wingtip are almost uniform. This allows the evolution of the complicated vortical flow structures. Around the trailing edge of the wingtip region, unnecessary grid concentration is avoided compared with the 6M grid (See Fig. 4 (b)). Although, grid size in chordwise direction has decreased to nearly 1/4 and the fine grid region has been extended, the overall increase in grid points is suppressed to approximately 3 times of that of the 6M grid.

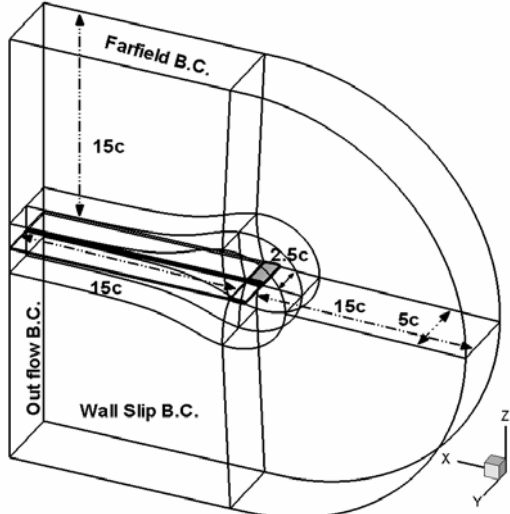
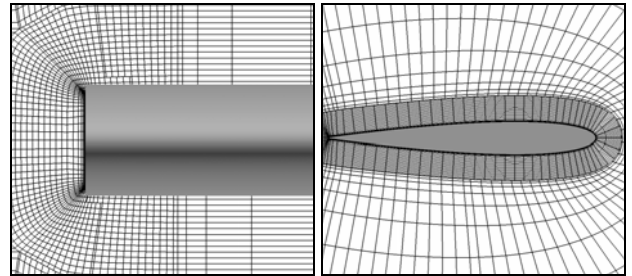


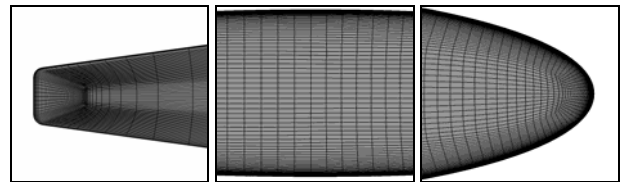
Fig. 2. Grid Topology and Boundary Conditions

Table 1 The Details of the Grids

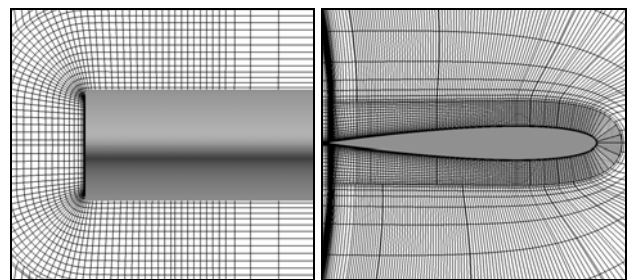
Grid	6M	20M
Total points	6 million	20 million
No of blocks	111	201
Grid points along Camber	190	408
Grid points at Maximum wing thickness	97	101
Grid points at TE	97	30



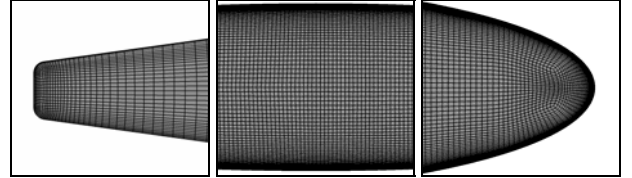
(a) Spatial grid distribution around the wingtip
(Every 3 points are drawn)



(b) Surface grid distribution on the wingtip
(All points are drawn)
Fig. 3. Coarse Grid (6M)



(a) Spatial grid distribution around the wingtip
(Every 3 points are drawn)



(b) Surface grid distribution on the wingtip
(All points are drawn)
Fig. 4. Fine Grid (20M)

2.3 CFD solver

Numerical methods used in the calculations are briefly described. Large-eddy simulation (LES) code, which is called UPACS-LES, is used in this research. This code is developed based on UPACS code [13-16], which is a standard CFD code in JAXA. The flow solver of the current version is based on a cell-centered finite-volume method on multi-block structured grids. The code is parallelized by a flexible domain decomposition concept and MPI. The

governing equations are the compressible Navier-Stokes equations. There are several options for the choice of turbulence modeling; LES mode, RANS mode, or LES/RANS hybrid mode.

Standard Smagorinsky model with $C_s=0.1$ is used for the LES computation [17] and the Spalart-Allmaras one equation model [18] is used for the RANS computation. In this study, the unsteadiness only around the wingtip is the region of interest, where wingtip noise is generated. In order to reduce the computational cost, the wingtip region is computed by LES and the rest of the region is calculated by the Spalart-Allmaras (S-A) one-equation model. The switching between LES and RANS regions are controlled by the switching function. In this study, the boundaries of LES and RANS are defined by planes at $y/c=-0.1$ and 0.15 for 6M and 20M grids, respectively.

The simulations were performed using characteristic boundary conditions along the far-field boundaries in the chordwise cross sectional plane, except for extrapolation from the interior at the downstream boundary. Slip-wall boundary condition is applied to the spanwise cross sectional planes and no-slip boundary conditions are imposed at the wing surface (See Fig. 2).

Zonal LES/RANS simulations are performed in the following procedures. First, RANS (S-A) computation is performed in order to obtain steady-state flowfield as an initial condition for the unsteady computations. Second, zonal LES/RANS computations are performed in order to obtain unsteady flow. The simulations were run over a long duration that consisted of 2 wing flow-through time units in order to minimize the transient effects. No acceleration was added in order to enforce the unsteadiness of the flow. And finally, unsteady computations are performed in order to obtain the flow statistics. In order to reduce the convergence error in the flow statistics, the simulations were run over 2 wing flow-through time units.

The computed results are assessed by changing the turbulence modeling and grid resolution. The details of the computations are summarized in Table 2. Case 1 and 2 are the

steady-state RANS computations using S-A model on 6M and 20M grids, respectively. The convection terms are discretized using the Roe scheme with 3rd-order MUSCL and no-limiter is imposed. First order time integration is performed by an implicit method using Matrix-Free Gauss-Seidel (MFGS) scheme [19] with local time stepping technique. The Courant-Friedrichs-Levy (CFL) number is set to 100 and computation is performed until convergence is achieved. Case 3 (6M grid) and 4 (20M grid) are zonal LES/RANS hybrid computations. High order schemes are used in the simulations in order to obtain the best resolution from the given grid. The convection terms are discretized using 6th-order compact scheme developed by Kobayashi [20]. The viscous terms are discretized using 2nd-order central scheme. In order to avoid numerical instability, 6th-order filter developed by Gaitonde-Visbal [21] is used with filter constant of $\alpha=0.45$. Second order time integration is performed by MFGS with 3 sub-iterations. The non-dimensionalized time steps using the chord length of the wing and sonic speed as reference values are set to $\Delta t=2 \times 10^{-4}$ and 10^{-4} for 6M and 20M grids, respectively. These values were chosen in order to satisfy the CFL condition ($CFL<1$) at most part of the wingtip region, excluding the boundary layer. This constrain must be satisfied in order to calculate the acoustic waves and vortices accurately inside the LES region.

Table 2 Computational Cases

	Turbulence Model	Grid	Scheme
Case 1	RANS (S-A)	6M	Roe 3 rd order
Case 2	RANS (S-A)	20M	Roe 3 rd order
Case 3	Zonal LES/RANS	6M	Compact 6 th order
Case 4	Zonal LES/RANS	20M	Compact 6 th order

3 Computational Results

First of all, the numerical data are validated by detail comparison between the experimental results. Both time-averaged and unsteady components are assessed. Especially, the effects

of the grid resolution to the power spectral density of pressure coefficient (C_p) are examined. Finally, using the validated data, detail flow structures around the wingtip are examined.

3.1 Validation of the Computed Results (Time-averaged Flow Field)

From the previous studies, it is well known that the flow field around wingtip is associated with dual vortex structure. Figure 5 shows the time-averaged vorticity magnitude iso-surface with cross sectional distribution of the streamwise vorticity around the wingtip. The vortex over the upper surface and that on the wingtip are termed primary and secondary vortex, respectively, in the established terminology [9]. However, these two vortices are rotating in the same direction. Thus, it is more appropriate to understand these two vortices as two independent primary vortices. In this study, these vortices are termed as upper and side vortices, respectively. These two primary vortices are generated from lower and upper edge of the wingtip and merge into a single tip vortex, as they move downstream.

The simulated flow field around the wingtip is compared with the experiment. Figure 6 shows the chordwise C_p distribution at two different locations. The C_p distribution along the camber line of the wingtip is shown in Fig. 6 (a). The RANS results are in good agreement with the experiment. A local minimum is observed around $x/c=0.5$, where the side vortex crosses the camber line. The C_p distribution along the wing cross section at $y/c=-0.0225$ (9mm from the wingtip) is shown in Fig. 6 (b). In this figure, two local minima can be seen after the suction peak near the leading edge. The peak at $x/c=0.3$ is caused by the upper vortex. As moving downstream, this vortex moves away from the upper surface (see Fig. 5), and local maximum appears around $x/c=0.6$. Going further downstream, a peak appears around $x/c=0.8$, where the upper vortex comes closer to the upper surface due to the influence of the side vortex (see Fig. 5). These tendencies are the same for all of the results.

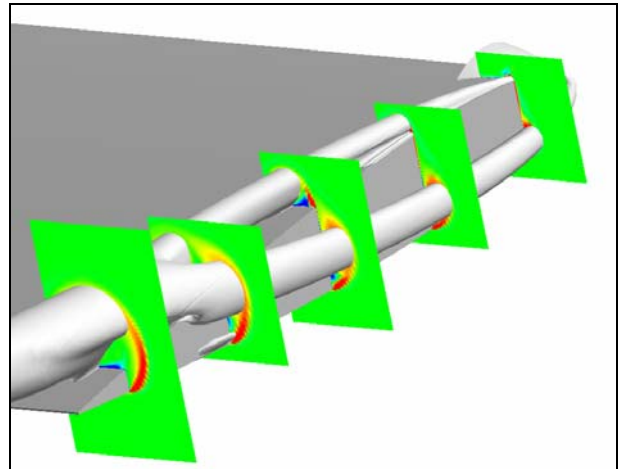


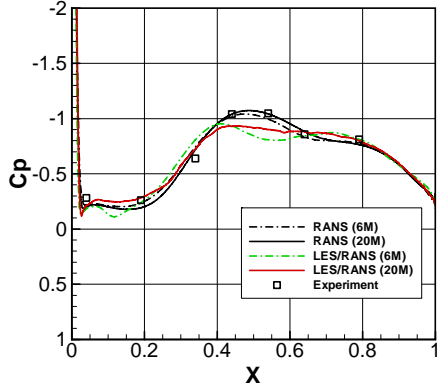
Fig. 5. Time-averaged Flow Field
Isosurface of vorticity magnitude with cross sectional distribution of streamwise vorticity (Case 1)

Figure 7 shows the streamwise velocity component distribution obtained by LES/RANS, as well as that of the particle image velocimetry (PIV) measurement data [11,12] at $x/c=0.5$ chordwise cross sectional plane. The velocity is normalized by the mean flow velocity and the same scale is used for all of the plotting. Since LES/RANS results are unsteady, time-averaged data are used. Two primary vortices are observed near the wingtip, one over the upper surface and another adjacent to the flat wingtip. Axial velocity within the vortex core can be greater (jet type) or less (wake type) than the freestream velocity [9]. All of the results show that the upper and side vortices are of jet and wake types, respectively.

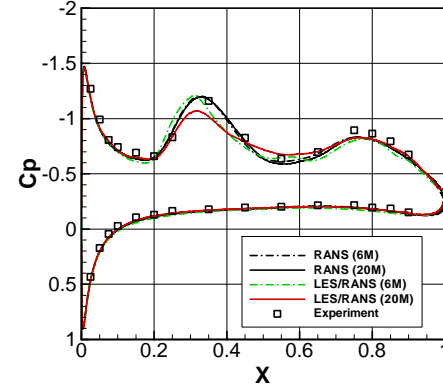
In order to perform qualitative comparison with the experimental data, streamwise velocity profile along line A and B are shown in Fig 8. The locations of the lines are given in Fig. 7 (a), where line A passes through the upper vortex horizontally and line B passes through the side vortex vertically. For RANS results, both lines collapse into the same line, and are consistent with the experimental data. Grid convergence is already obtained for 6M grid. Along line A, local maximum are observed around $y/c=-0.03$. For LES/RANS 6M results, the deviation from the experiment and RANS is significant. By increasing the grid points in streamwise direction, improvement in prediction accuracy can be clearly observed. The plot by LES/RANS

20M are much closer to the experimental results compared with 6M result. Along line B, two local minima are observed. The minima at $z/c = -0.05$ and -0.08 are caused by the primary and the secondary vortex at the side of the wingtip. In

this case, secondary vortex is rotating in opposite direction of the primary vortex. Once again, the LES/RANS 6M result under predicts the level of the local minima, and improvement can be observed by increasing the grid resolution.

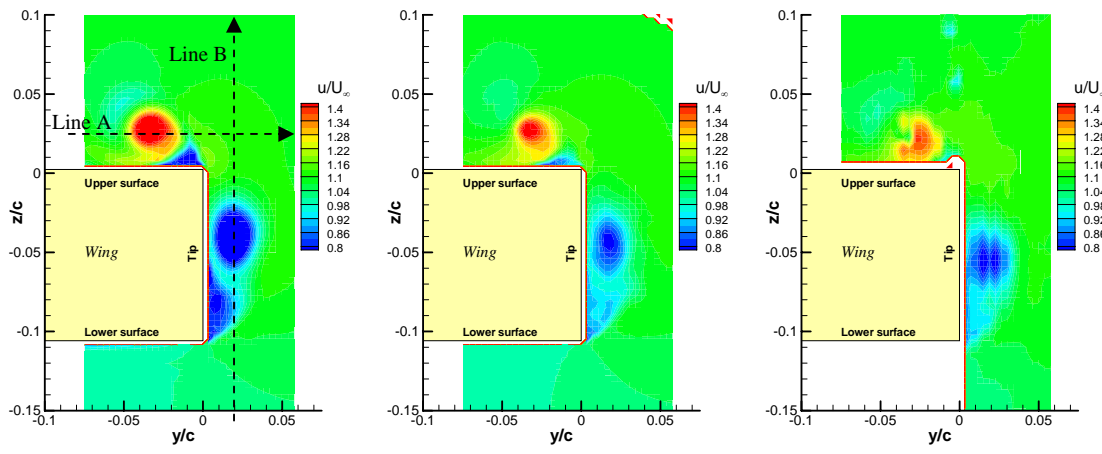


(a) Camber line



(b) $y/c = -0.0225$

Fig. 6. Cp Distribution in Chordwise Direction

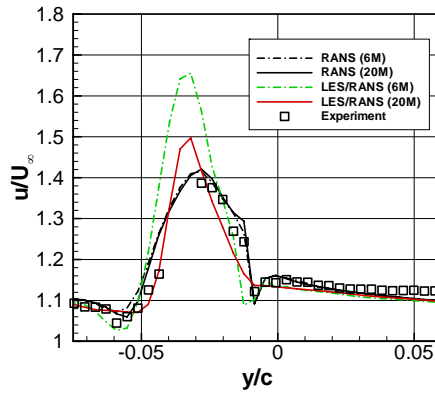


(a) LES/RANS 6M

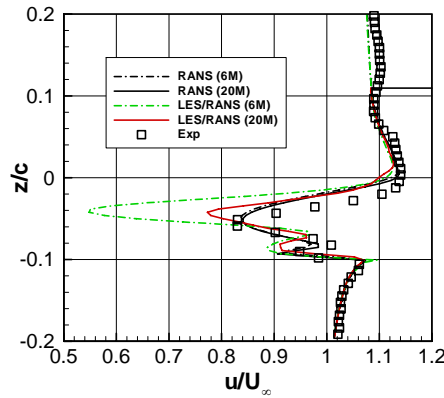
(b) LES/RANS 20M

(c) Experiment

Fig. 7. U-velocity Component on $x/c = 0.5$ Plane



(a) Line A



(b) Line B

Fig. 8. Streamwise Velocity Profile

3.2 Validation of the Computed Results (Unsteady Flow Field)

Figure 9 compares the power spectral density (PSD) of C_p on the upper surface ($y/c=0.0125$ which is 5mm from the wingtip) at three locations. At $x/c=0.05$, the level of the PSD is low through out all frequency range in the experiment. This tendency is computed by both LES/RANS 6M and 20M. At $x/c=0.2$, the PSD pattern varies between the grids. In the experiment, broad peak is observed at 5 kHz. This peak is reproduced by the results from LES/RANS 20M while the estimated peak level is slightly higher than the experiment. As going further downstream to $x/c=0.65$, the level of the low frequency broadband component increases. The results by the 6M grid fails to predict the level of PSD around the frequency of 1 to 5 kHz, but it is captured by the 20M grid. By increasing

the grid points, better agreement is obtained compared with the experimental results.

Figure 10 shows the instantaneous iso-surface of vorticity magnitude colored by vorticity in vertical direction. The results of LES/RANS 6M and 20M are shown in Fig. 10 (a) and (b), respectively. In Fig 10 (a), the most of the vortical structures are limited to the cross sectional plane, because the grid size in the chordwise direction is coarser than that of the chordwise cross sectional plane. On the other hand, complicated flow structure around the wingtip is visualized in Fig. 10 (b). By increasing the grid points in chordwise direction, significant difference in the vortical flow field can be observed. Although, the dual vortex system at the wingtip region is oriented to the chordwise direction, high resolution grid is required to allow the vortices to evolve in all directions.

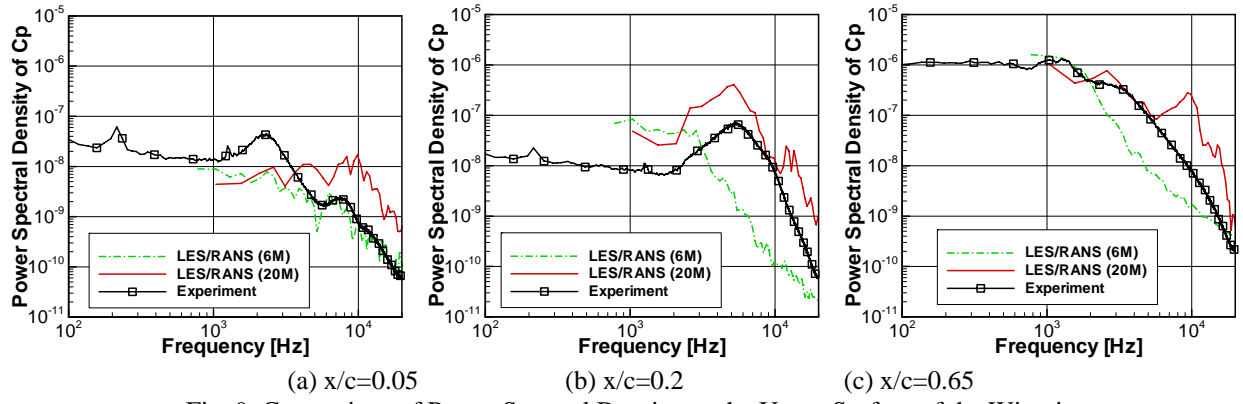


Fig. 9. Comparison of Power Spectral Density on the Upper Surface of the Wingtip

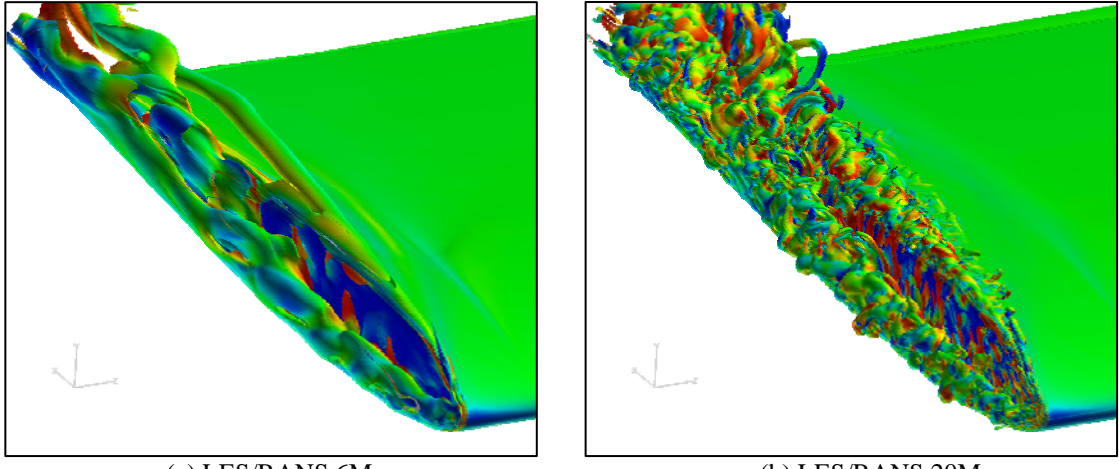


Fig. 10. Instantaneous Iso-surface of Vorticity Magnitude Colored by Vorticity in Vertical Direction

3.3 Detail Observation of the Flow Field

Now, detail observation of the flow field will be performed using the LES/RANS 20M data. Figure 11 show the TKE distribution derived at $x/c=0.5$, 0.7 and 0.95 cross sectional planes. High TKE regions are observe at the core of the upper and side vortices as shown in Fig. 11 (a) and (b). Near the trailing edge, where the merging of the dual vortex is finished, high TKE region is distributed over the upper surface of the wing (See Fig. 11(c)).

Fig. 12 and 13 shows the surface and spatial pressure fluctuation around the wingtip. The surface pressure fluctuation is significant especially on the surface adjacent to the side vortex. From Fig. 13 (a), propagation of acoustic waves is clearly visualized. The frequency of this acoustic wave is estimated from the wave length and it is approximately 10 kHz. From Fig.

13 (b) and (c), concentric rings of acoustic waves can not be observed like as in Fig 13 (a). This indicates that the noise source of this frequency is distributed along the chordwise direction of the wingtip.

Since the mean flow Mach number is small ($M=0.175 \ll 1$), the surface dipoles dominates the far field noise. Thus, Curle's equation [22] based on the Lighthill's analogy is used to estimate the far field SPL. One important reminder is that for frequency higher than 1 kHz, the wing can not be assumed to be acoustically compact. Thus, there might be some error in this frequency range. The observer location is directly below the leading edge of the wingtip at the distance of $10c$. The 1/3 octave band results are shown in Fig. 14. The peak around 10 kHz are observed and this is consistent with the pressure pulse observed in Fig. 13.

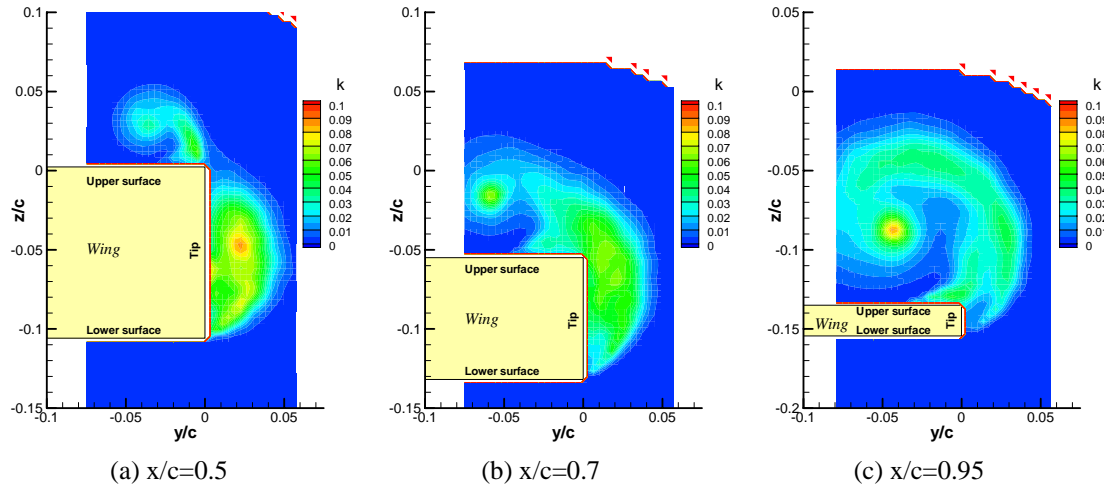


Fig. 11. TKE on three cross sectional planes (LES/RANS 20M result)

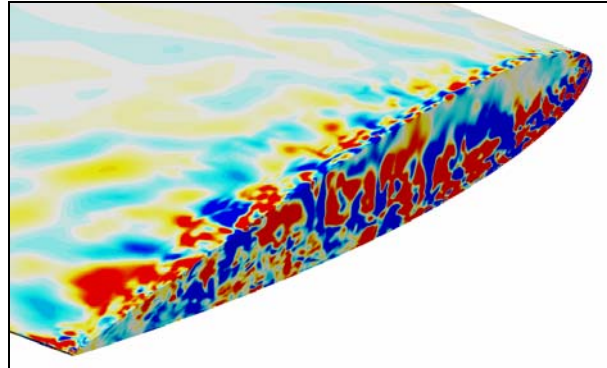


Fig. 12. Instantaneous Surface Pressure Fluctuation Distribution

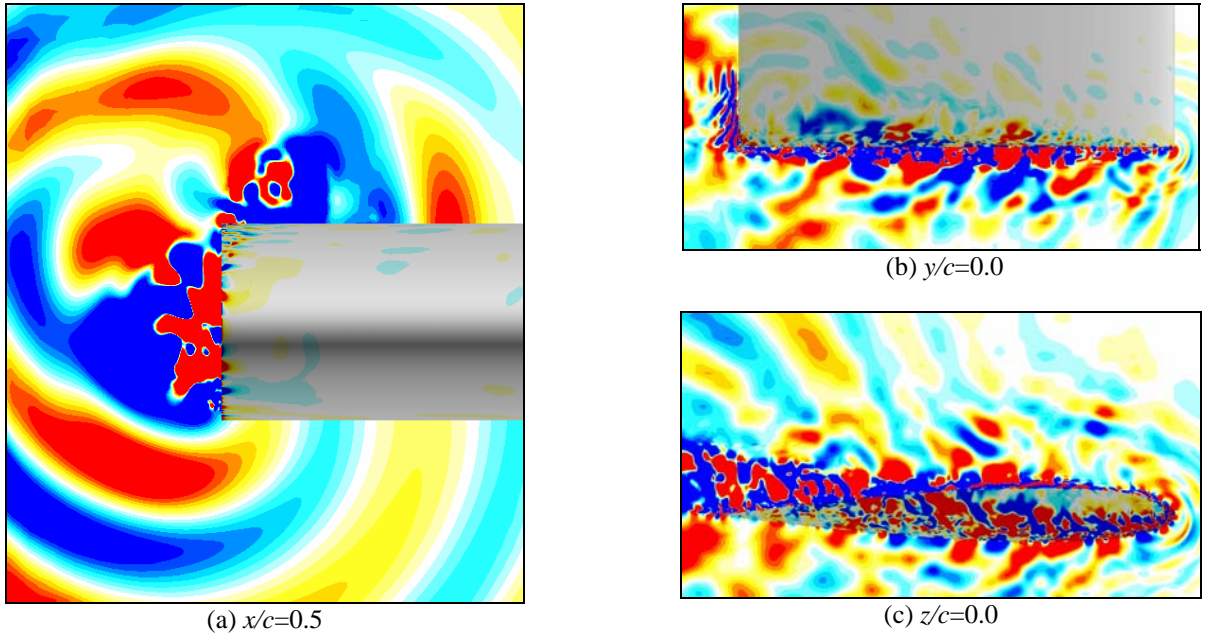


Fig. 13. Instantaneous Pressure Fluctuation Distribution around the Wingtip

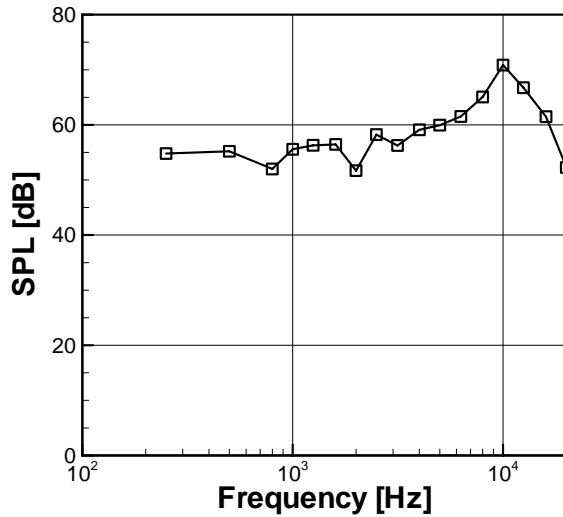


Fig. 14. Far-field Noise Estimation using Curle's Equation (1/3 octave band)

4 Conclusions

A Flow around NACA0012 wingtip was solved using zonal LES/RANS hybrid method.

The computational results were validated by comparing with the experimental data and grid dependency studies were performed. By using relatively uniform grid around the wingtip region, the prediction accuracy of both time-averaged and unsteady components have increased.

Using the validated data, flow physics around the wingtip were examined. The current result on the fine grid shows that the flow is much more complicated than it was reported in the previous studies. Not only the dual vortex structure in streamwise direction, but also the small vortices directed to omni-direction were important contributors to the overall flow field. Furthermore, acoustic waves propagating from the wingtip and far field SPL were obtained successfully.

References

- [1] Hardin, J. C., "Airframe self-noise: Four years of research; aircraft noise reduction for commercial aircraft," NASA-TM-X-73908, Jul 1976.
- [2] Streett, C. L., Lockard, D.P., Singer, B.A., Khorrami, M.R., and Choudhari, M.M., "In Search of the Physics: The Interplay of Experiment and Computation in Airframe Noise Research; Flap-Edge Noise" AIAA Paper 2003-977, Jan. 2003.
- [3] Choudhari, M., and Khorrami, M. R., "Computational Study of Porous Treatment for Altering Flap Side-Edge Flow Field", AIAA Paper 2003-3113, May 2003.
- [4] Streett, C.L., "Numerical Simulation of Fluctuations Leading to Noise in a Flap-Edge Flowfield", AIAA Paper 98-0628, Jan. 1998.
- [5] Street, C.L. "Numerical Simulation A Flap-edge Flowfield", AIAA paper 98-2226, June 1998.
- [6] Takallu, M.A., and Laflin, K. R. "Reynolds-Averaged Navier-Stokes Simulations of Two Partial-Span Flap Wing Experiments" AIAA Paper 98-0701, Jan. 1998.
- [7] Khorrami, M. R., Singer, B. A., Radeztsky, Jr., R. H. "Reynolds Averaged Navier-Stokes Computations of Flap Side-Edge Flow Field", AIAA Paper 98-0768, Jan. 1998.
- [8] Cummings, R. M., Morton, S. A. and Forsythe, J. R., "Detached-Eddy Simulation of Slat and Flap Aerodynamics for High-Lift Wing", AIAA Paper 2004-1233, Jan. 2004.
- [9] McInerny, S. A., Meecham, W. C., and Soderman, P. T., "Pressure Fluctuations in the Tip Region of a Blunt-Tipped Airfoil", AIAA Journal, Vol.28, No.1, 1990, pp. 6-13
- [10] Imamura, T., Enomoto, S., Kato, H., Yokokawa, Y., and YAMAMOTO, K., " Numerical Simulation of NACA0012 Wingtip Flow Leading to Noise Generation ", AIAA paper 2005-2864 11th AIAA/CEAS Aeroacoustics Conference
- [11] Watanabe, S., and Kato, H., "Stereo PIV Applications to Large-Scale Low-Speed Wind Tunnels", AIAA Paper 2003-0919 Jan. 2003.
- [12] Watanabe, S., Kato, H., Lei, Z, Imamura, T., and Enomoto, S. "CFD code Validation via Particle Image Velocimetry (PIV)", Proceedings of Aerospace Numerical Simulation Symposium 2004, JAXA SP 2004 (in Japanese).
- [13] Yamane, T., Yamamoto, K., Enomoto, S., Yamazaki, H., Takaki, R., and Iwamiya, T., "Development of a Common CFD Platform - UPACS -," in Parallel Computational Fluid Dynamics - Proceedings of the Parallel CFD 2000 Conference, Trondheim, Norway, Elsevier Science B. V., 2001, pp. 257-264.
- [14] Takaki, R., Yamamoto, K., Yamane, T., Enomoto, S., and Mukai, J., "The Development of the UPACS CFD Environment," in High Performance Computing Proceedings of 5th International Symposium, ISHPC 2003, Ed. Veidenbaum et al., Springer, 2003, pp307-319.
- [15] Murayama, M., Yamamoto, K., and Kobayashi, K., "Validation of Flows on High-Lift Configurations by Structured- and Unstructured- Mesh Method", AIAA Paper 2005-1226, Jan. 2005.
- [16] Yamamoto, K., Ochi, A., Shima, E., and Takaki, R., "CFD Sensitivity of Drag Prediction on DLR-F6 Configuration by Structured Method and Unstructured Method," AIAA Paper 2004-0398, Jan. 2004.
- [17] Smagorinsky, J., "General Circulation Experiments with the Primitive Equations", Mon. Weath. Rev., Vol.91, No.3, pp.99-164.
- [18] Spalart, P.R., and Allmaras, S. R., "A One-Equation Turbulence Model for Aerodynamic Flows", AIAA Paper 92-0439, Jan. 1992.
- [19] Shima, E., "A Simple Implicit Scheme for Structured/Unstructured CFD," Proceedings of 29th Fluid Dynamics symposium, Hokkaido, Japan, 1997, pp.325-328. (in Japanese)
- [20] Kobayashi, M. H. "On a Class of Pade Finite Volume Methods", J. Comp. Phys. 156 1999 , pp.127-180.
- [21] Gaitonde, D. V., and Visbal, M. R., "Pade-Type Higher Order Boundary Filters for the Navier-Stokes Equations", AIAA Journal, Vol.38, No.11, 2000, pp2103-2112.
- [22] Curle, N., "The Influence of Solid Boundaries upon aerodynamics Sound", Proc. Roy. Soc. A231, p.505-514, (1955)